

# LME-MPM applied to quasi-brittle fracture.

Miguel Molinos<sup>a1</sup>, Pedro Navas<sup>a2</sup>, Diego Manzanal<sup>a</sup>, and Manuel Pastor<sup>a</sup>

<sup>a</sup> *ETSI Caminos, Canales y Puertos, Universidad Politécnica de Madrid.  
c. Prof. Aranguren 3, 28040 Madrid, Spain*

---

## Abstract

The objective of this work is to introduce an alternative technique to address the fracture process of brittle and quasi-brittle materials under the Material Point Method (MPM) framework. With this purpose the eigensoftening algorithm, developed originally for the Optimal Transportation Meshfree (OTM) approximation scheme, is extended to the MPM with the aim of presenting a suitable alternative to the existing fracture algorithms developed for the MPM. The good fitting in the predictions made by the eigensoftening algorithm against both analytical and experimental results proofs the well performance of the method when challenging applications are to modeled.

*Keywords:* Quasi brittle fracture, Local-*Max-Ent* approximation, Material Point Method, Solid Dynamics

---

## 1. Introduction

The presence of cracks is a violation of the continuity requirement of the Finite Element Method (FEM). To overcome this issue, numerous numerical artifacts have been proposed with the aim of reproducing such a  
5 complex behaviour. These techniques vary from the employment of cohesive approaches [1, 2], to the gradual insertion of cohesive elements [3, 4, 5] at solid elements boundaries, or handling arbitrary crack paths by level set representation of the fracture surface [6]. The simulation of fracture propagation in a more accurate and effective way can be considered as one of  
10 the ongoing goals of the development of novel spatial discretization methods like meshfree techniques. Some examples of it are the Material Point Method (MPM) [7, 8, 9, 10], the Element-Free Galerkin Method (EFGM) [11, 12, 13, 14], the Smoothed Particle Hydrodynamics (SPH) [15, 16], the

---

<sup>1</sup>Corresponding author: m.molinos@alumnos.upm.es

<sup>2</sup>Corresponding author: p.navas@upm.es

Optimal Transportation Meshfree (OTM) [17, 18, 19, 20] or Peridynamics  
15 [21, 22] among others.

Regarding MPM, fracture has been treated numerically through two different ways. On the one hand, the “CRACKs with Material Points (CRAMP)” is proposed [9, 23]. The basis of this methodology consist of the removal of  
20 the restriction of the single-valued velocity field close to the crack through, at least, two sets of nodes. In this method, different labels are assigned to the material points and nodes to distinguish if they are in the same side of the crack or not. Under this approach, crack surface is described with line segments in 2D and triangle patches in 3D cases. The chosen criteria for crack  
25 propagation is based on such parameters as energy release rate analyzed by Tan & Nairn (2002)[24], and the stress intensity factor or the J-integral discussed by Guo & Nairn (2004)[25]. On the other hand, the foundation of the second approach is the introduction of failed material points to describe the crack evolution. In these methods, the formation of failed points describes  
30 the nucleation of cracks, and thereafter its propagation and branching. Consequently, the position of the crack does not need to be explicitly stated. This fact represents significant advantages over the “CRAMP”. Under this approach, the prediction of failure evolution is computed with a decohesion model, which has been discussed by Chen *et al.*[10] and Schreyer *et al.*[7].  
35 Successful simulations are provided within the framework of the fracture of brittle materials by Chen *et al.* [8, 26] and Sulsky & Schreyer [27].

Similar to this approach, Schmidt *et al.* [28] introduced the concept of eigenfracture, where crack sets are approximated by means of eigen-deformations,  
40 which enable the material to develop displacement jumps at no cost of local elastic energy. Later, the eigenerosion approach to brittle fracture was carried out by Pandolfi *et al.* [29, 19]. In this technique, the concept of “erosion” of the material point is depicted, being the material point able to remain intact or become completely failed or eroded, when no loading capacity is  
45 bore. This method has been successfully applied to simulate high complex phenomena such as dynamic fragmentation of metals [20]. Recently, Zhang *et al.* [30] adopted the eigenerosion to resolve the dynamic fracture of brittle materials in the MPM framework. Nonetheless, when quasi-brittle materials are simulated though this approach, the results exhibit an overestimation  
50 of tensile stress and strain peaks. Furthermore, since the work of Zhang *et al.* [30] is made with conventional MPM/GIMP, stress oscillations are to be faced.

To overcome the limitations observed in the EigenMPM [30], the present

55 research proposes the eigensoftening algorithm developed by Navas *et al.* [31, 32] for the OTM framework and engineered for quasi-brittle materials. Inspired in the concept of the crack band model [33], since energy dissipation is performed through the softened (or failed) volume, this methodology is able to capture the gradual rather than abrupt dissipation of the fracture  
60 energy. Moreover, in order to mitigate stress oscillations as well as to deal with tensile instabilities, such those that occurs when particles crosses an element boundary, the work of Molinos *et al.* [34] is followed. The traditional MPM technique is enhanced through the Local Maximum-Entropy (LME) approximation technique [35] for the spatial discretization as well as  
65 a explicitly MPM Newmark Predictor-Corrector (NPC) scheme is derived for the time discretization.

The paper is structured as follows. First meshfree methodology, eigen-erosion and eigensoftening algorithms are presented in Section 2. Then, both  
70 approaches are compared and verified by means of comparisons with analytical and experimental results in Section 3. Finally, relevant conclusions are exposed in Section 4.

## 2. The meshfree methodology

The aim of this section is to describe and introduce some special tech-  
75 niques required to face the fracture problem under the MPM framework. In consequence, this section is structured as follows: first, in 2.1, the Newmark Predictor-Corrector (NPC) algorithm for the MPM will be exposed; next the LME approximants are introduced in 2.2 as an accurate alternative technique to interpolate data between particles and nodes, and finally fracture  
80 algorithms based on the eigendeformation concept are presented in 2.3.

### 2.1. The MPM time integration : A Newmark Predictor-Corrector scheme

The MPM [36] is a meshfree Lagrangian-Eulerian method where moving material points, henceforth in this research, particles ( $\square_p$ ) will carry on all the physical information of the local state ( $\sigma_p, \varepsilon_p$ ) and a set of fixed background nodes ( $\square_I$ ) will be introduced to compute the balance of momentum equation. Since the MPM possesses the advantages of both Lagrangian and Eulerian descriptions, no element distortion takes place in the MPM. Therefore, it is an appropriate and efficient method to solve problems with moving discontinuities such as fracture evolution.

Without loosing generality, the MPM algorithm can be described with three main steps: (i) a variational recovery process, where particle data is projected to the grid nodes, (ii) an Eulerian step, where balance of momentum

equation is expressed as a nodal equilibrium equation in a FEM-like procedure, and finally (iii) a Lagrangian advection of the particles. In the present research, an explicit predictor-corrector time integration scheme is adopted. The purpose of this choice is motivated due to its proved robustness and stability for dynamic computations. In the first stage, the nodal velocity predictor  $\vec{v}_I^{k+1}$  is computed through nodal velocities  $\vec{v}_I$  and accelerations  $\vec{a}_I$  and evaluated in the  $k$  time step,

$$\vec{v}_I^{k+1} = \frac{N_{Ip}^k m_p (\vec{v}_p^k + (1 - \gamma) \Delta t \vec{a}_p^k)}{\mathbf{m}_I^{k+1}} . \quad (1)$$

Where  $\gamma$  is an user-defined parameter (typically adopted as 0.5),  $\mathbf{m}_I$  represents the lumped mass matrix, and  $N_{Ip}^k$  is the nodal contribution of the shape function evaluated in the particle coordinates  $\vec{x}_p^k$ . This way of computing the nodal predictor is numerically stable as well as minimises the computational effort. Once nodal velocities are obtained, the essential boundary conditions are imposed. After that, an Eulerian phase is computed in the set of nodes in a FEM-like way, where nodal forces  $\vec{f}_I^{k+1}$  are computed through the equilibrium equation. Next the nodal velocities are corrected in a *corrector* stage:

$$\vec{v}_I^{k+1} = \vec{v}_I^{pred} + \gamma \Delta t \frac{\vec{f}_I^{k+1}}{\mathbf{m}_I^{k+1}} . \quad (2)$$

Finally, in order to update the particles, those are advected in the Lagrangian stage as

$$\vec{a}_p^{k+1} = \frac{N_{Ip}^k \vec{f}_I^k}{\mathbf{m}_I^k} , \quad (3)$$

$$\vec{v}_p^{k+1} = \vec{v}_p^n + \Delta t \frac{N_{Ip}^k \vec{f}_I^k}{\mathbf{m}_I^k} , \quad (4)$$

$$\vec{x}_p^{k+1} = \vec{x}_p^n + \Delta t N_{Ip}^k \vec{v}_I^k + \frac{1}{2} \Delta t^2 \frac{N_{Ip}^k \vec{f}_I^k}{\mathbf{m}_I^k} . \quad (5)$$

The complete pseudo-algorithm it is summarised in Appendix A.

## 2.2. Spatial interpolation technique : Local Maximum-Entropy approximants

Local Maximum-Entropy (LME) approximation scheme was introduced by Arroyo & Ortiz (2006)[35] as a bridge between finite elements and meshfree methods. The key idea under this interpolation technique is the interpretation of each nodal value  $N_I$  as a probability. Related with this definition,

two important limits are introduced. First the maximum-entropy (*max-ent*) limit, which ensures a *unbiased statistical inference* based on the nodal data as states the Jayne's[37] principle of *maximum entropy*. And second the Delaunay triangulation that warranties the *least width* shape function support. To reach **delete to** a compromise between two competing objectives, a Pareto set is defined as,

$$\begin{aligned} (\text{LME})_\beta \text{ For fixed } \vec{x} \text{ minimise } f_\beta(\vec{x}_p, N_I) &:= \beta U(\vec{x}_p, N_I) - H(N_I) \\ \text{subject to } &\begin{cases} N_I \geq 0, \text{ I}=1, \dots, n \\ \sum_{I=1}^{N_n} N_I = 1 \\ \sum_{I=1}^{N_n} N_I \vec{x}_I = \vec{x} \end{cases} \end{aligned}$$

where  $H(N_I)$  is the entropy of the system of nodes following the definition given by Shannon (1948) [38], the shape function width is defined as  $U(\vec{x}_p, N_I) := \sum_I N_I |\vec{x}_p - \vec{x}_I|^2$ , and  $\beta$  is a regularization o *thermalization* parameter such that for Pareto optimal solutions  $\beta \in (0, \infty)$ . Notice that  $\beta$  has units of  $[L]^{-2}$ , therefore it can be controlled by adjusting a dimensionless parameter<sup>3</sup>,  $\hat{\gamma} = \beta h^2$ , where  $h$  is defined as a suitable measure of the nodal spacing. With the restrictions of the Pareto set, the unique solution of the local *max-ent* problem  $\text{LME}_\beta$  is,

$$N_I^*(\vec{x}) = \frac{\exp \left[ -\beta |\vec{x} - \vec{x}_I|^2 + \vec{\lambda}^* \cdot (\vec{x} - \vec{x}_I) \right]}{Z(\vec{x}, \vec{\lambda}^*)}, \quad (6)$$

where  $Z(\vec{x}, \vec{\lambda}^*)$  is the *partition function* defined as,

$$Z(\vec{x}, \vec{\lambda}) = \sum_{I=1}^{N_n} \exp \left[ -\beta |\vec{x} - \vec{x}_I|^2 + \vec{\lambda} \cdot (\vec{x} - \vec{x}_I) \right], \quad (7)$$

and a Lagrange multiplier  $\vec{\lambda}^*$  such minimise the function  $\log Z(\vec{x}, \vec{\lambda})$ . The tra-  
85 ditional way to compute the optimal value of  $\vec{\lambda}^*$  is through a Newton-Raphson procedure, or in more challenging scenarios by a combination of the Newton-Raphson and the Nelder-Mead Simplex algorithms [32]. Nonetheless, since

---

<sup>3</sup>To avoid confusion with the  $\gamma$  parameter of the NPC, the dimensionless parameter defined in Arroyo & Ortiz [35] as  $\gamma$  will be represent by  $\hat{\gamma}$  to preserve as much as possible the original notation.

finite strains are not involved in the present research, Newton-Raphson is an enough efficient method. For an uniform nodal spacing,  $\beta$  can be considered  
 90 constant, thus first derivatives of the interpolation technique  $\nabla N_I^*$  can be obtained by evaluating the following expression

$$\nabla N_I^* = -N_I^* (\mathbf{J}^*)^{-1} (\vec{x} - \vec{x}_I) \quad (8)$$

where  $\mathbf{J}$  is the Hessian matrix, defined by

$$\mathbf{J}(\vec{x}, \vec{\lambda}, \beta) \equiv \frac{\partial \vec{r}}{\partial \vec{\lambda}}, \quad (9)$$

$$\vec{r}(\vec{x}, \vec{\lambda}, \beta) \equiv \frac{\partial \log Z(\vec{x}, \vec{\lambda})}{\partial \vec{\lambda}} = \sum_I^{N_n} p_I(\vec{x}, \vec{\lambda}, \beta) (\vec{x} - \vec{x}_I). \quad (10)$$

An additional remark concerning the support of the interpolation function is that, in practice, the value of  $N_I$  decay exponentially following  $\exp(-\beta \vec{r})$ .  
 95 In this sense, a good practice is to truncate it under a tolerance (typically around  $10^{-6}$ ) that would ensure a reasonable range of neighbours, see [35] for details. This tolerance defines a limit value of the influence radius to find the neighbour nodes of a given integration point.

### 2.3. Fracture modelling approach

100 Within the context of MPM formulation, fracture can be modelled by failing particles according to a suitable failure criterion. When material points are failed, they are assumed to have null stress tensor. To reproduce this behaviour in the present research, the eigensoftening algorithm is introduced in the MPM framework as an alternative approach to the decohesion model  
 105 [10, 7]. The eigensoftening concept was originally developed by Navas *et al.* (2017)[31] as an extension for quasi-brittle materials of the eigenerosion proposed by Pandolfi & Ortiz (2012)[29] for fracture of brittle materials. The evaluation of both approaches [31] against experimental measures show that the eigenerosion algorithm significantly overestimates the tensile stress and the strain peaks, meanwhile eigensoftening captures the forces and crack  
 110 patterns accurately. Furthermore, the accuracy of this algorithm has been proven for complex fracture patterns such as the ones obtained with fiber reinforces concrete (FRC), [39].

The key idea behind the eigenerosion algorithm is the computation of the

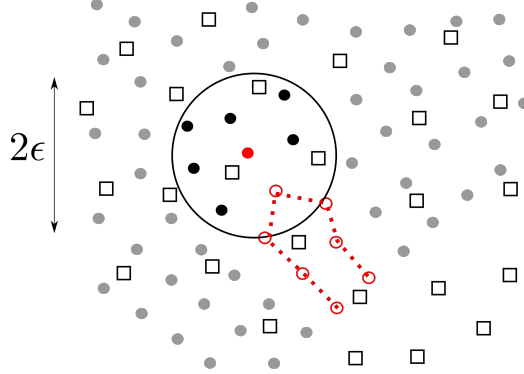


Figure 1: Scheme of a linear cohesive law, where the shaded area is  $G_f$ ,  $f_t$  is the tensile strength, and  $w_c$  is the critical opening displacement.

energy-release rate attendant to the failure of material point  $p$ ,

$$G_p^{k+1} = \frac{C_\epsilon}{m_p^{k+1}} \sum_{x_q^{k+1} \in B_\epsilon(x_p^{k+1})} m_q W_q^{k+1} \quad (11)$$

$$m_p^{k+1} = \sum_{x_q^{k+1} \in B_\epsilon(x_p^{k+1})} m_q \quad (12)$$

where  $B_\epsilon(x_p^{k+1})$  is a  $n$ -dimensional sphere of radius  $\epsilon$  centered at  $x_p^{k+1}$ . The particles which lie under this sphere are known as the  $\epsilon$ -neighborhood of the material point (see [29]). This concept is conveniently sketched in Figure 1. Other parameters are the mass of the neighborhood  $m_p^{k+1}$ , the current free-energy density per unit mass  $W_q^{k+1}$  and the normalizing constant  $C_\epsilon$ , which also defines the  $\epsilon$ -neighborhood size, being  $\epsilon = C_\epsilon h$ , and  $h$  is a measure of the distance between nodes.

The failure criterion consist of considering that a material point is failed when  $G_p^{k+1}$  surpasses the critical energy release rate that measures the material-specific energy,  $G_F$ . The convergence of this approach has been analyzed by Schmidt *et al.* (2009)[28], who proved that  $G_F$  converges to the Griffith fracture when the discretization size tends to zero. It is necessary to point out that, when a material point overpass the critical energy, its contribution to the internal forces vector is set to zero, but its contribution to the mass matrix is preserved.

As can be noticed, the eigenerosion algorithm relies over an energetic failure criterion. Because of this, unrealistic stress concentration (higher than tensile strength) appears in quasi-brittle materials [31]. To overcome this limitation, the aforementioned authors proposed the concept of eigensoften-

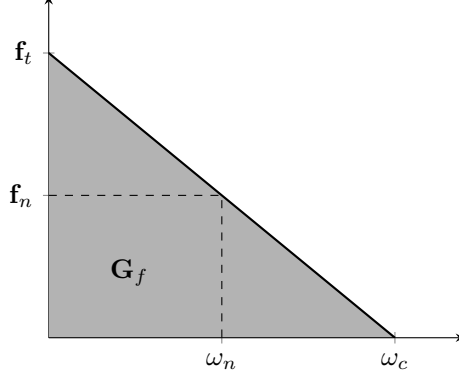


Figure 2: Scheme of a linear cohesive law, where the shaded area is  $G_f$ ,  $f_t$  is the tensile strength, and  $w_c$  is the critical opening displacement.

ing to take into account the gradual failure in quasi-brittle materials. The idea behind this concept is inspired in the cohesive fracture. This gradual failure criterion is plotted in figure , where a linear decreasing cohesive law is presented to illustrate the concept earlier described. In the picture, the shaded region represents the static fracture energy per unit of area,  $G_F$ . Notice how a cohesive crack appears when the maximum tensile strength,  $f_t$ , is reached. Once the crack,  $w_n$ , reaches the value of the critical crack opening,  $w_c$ , a stress-free crack is attained. For the eigensoftening algorithm, a strength criterion for crack initialization was adopted. [Particularly the maximum principal stress theory for brittle fracture was considered in \[31\], this allows to quantify the variation of the averaged strain energy density in the  \$\epsilon\$ -neighborhood of the material point  \$\vec{x}\_p^{k+1}\$  as](#)

$$\delta W_{\epsilon,p} = \frac{\partial G_p}{C_\epsilon} = \frac{1}{m_p} \sum_{x_q^{k+1} \in B_\epsilon(x_p^{k+1})} m_q \sigma_{q,I} \delta \varepsilon_q, \quad (13)$$

where  $\sigma_{q,I}$  is the maximum principal stress of each material point in the  $\epsilon$ -neighborhood. At this point, an *effective* strain  $\varepsilon_q$  is introduced in order to obtain the variation of the local strain energy as  $\delta W_q = \sigma_{q,1} \delta \varepsilon_q$ . Now, with the assumption that the effective strain of each material point at every time step is constant in the neighborhood of  $\vec{x}_p^{k+1}$ , the equation (13) can be simplified to

$$\delta W_{\epsilon,p} = \frac{\delta \epsilon_p}{m_p} \sum_{x_q^{k+1} \in B_\epsilon(x_p^{k+1})} m_q \sigma_{q,I}. \quad (14)$$



Consequently, it is possible to define an equivalent critical stress at the material point  $\vec{x}_p^{k+1}$  as

$$\sigma_{\epsilon,p} = \frac{1}{m_p} \sum_{x_q^{k+1} \in B_\epsilon(x_p^{k+1})} m_q \sigma_{q,I}, \quad (15)$$

where  $m_p$  is the total mass of the  $\epsilon$ -neighborhood, defined similarly to the eigenerosion method (Eq. (12)). The equivalent critical stress leads to a definition of the averaged strain energy in terms of the averaged strain as  $\delta W_{\epsilon,p} = \sigma_{\epsilon,p} \delta \epsilon_p$ . The softening behaviour is activated once  $\sigma_{\epsilon,p}^{k+1}$  surpasses the tensile strength,  $f_t$ . This consists of a reduction of the internal forces as,

$$f_I^{int} = \sum_p (1 - \chi_p) \sigma_p^{k+1} \cdot \text{grad}(N_{Ip}) \Omega_p \quad (16)$$

where  $\chi_p$  and  $\Omega_p$  are respectively the damage or softening variable and the volume for each material point  $p$ .  $\chi_p$  is any function, taking values between zero (an intact material) and one (completely failed material points), that relates the crack opening and the residual strength. To calculate it, typical shapes of cohesive laws such as linear, bilinear or exponential, may be employed. For the case of a linear softening such the sketched one in the Figure 2.3,  $\chi_p$  is computed as,

$$1 - \chi = \frac{f_n}{f_t} = 1 - \frac{w_n}{w_c} \rightarrow \chi = \frac{w_n}{w_c}. \quad (17)$$

Analogous to the crack band model presented by Bazant [33], Navas *et al.* [39] [31] introduced a band width parameter  $h_\epsilon$  in order to relate the crack opening with the strain. Concerning this parameter, a typical value between two and four times the maximum size of the aggregates is adopted in the case of concrete as brittle material. The effective fracture strain  $\varepsilon_{\epsilon,f}$  is defined as the difference between the strain at crack initialization,  $\varepsilon_1(\vec{x}_p^0)$ , and the current strain,  $\varepsilon_1(\vec{x}_p^{k+1})$ , for a material point  $p$ . Also,  $\varepsilon_{\epsilon,f}$  can be represented as the current crack opening  $w_n$  within the band width  $h_\epsilon$ . Therefore,

$$\varepsilon_{\epsilon,f} = \varepsilon_1(\vec{x}_p^{k+1}) - \varepsilon_1(\vec{x}_p^0) = \frac{w_n}{h_\epsilon} \quad (18)$$

Introducing (18) in (17), the damage variable can be computed as,

$$\chi = \frac{\varepsilon_{\epsilon,f} h_\epsilon}{w_c}. \quad (19)$$

The function of  $\chi$  presented in (19) represents a linear softening behaviour. For a general case, the damage variable can be expressed in terms of the following variables,

$$\chi = \chi(\varepsilon_{\epsilon,f}, h_{\epsilon}, f_t, w_c, G_f) \quad (20)$$

Implementation details can be consulted in Appendix B.

#### 2.4. $\epsilon$ -neighbourhood reconstruction : A node-linked method

The construction of the  $\epsilon$ -neighbourhood is a major issue of the proposed methodology. Since this operation could be extremely demanding, optimal numerical implementation should be employed. In opposite with the Cell-linked method proposed by Allen & Tildesley [40] where the definition of a numerical tolerance is required for auxiliar algorithms like Crossing Number [41] or Correct Even-Odd [42], the proposed methodology adopted herein is linked to the shape function neighbourhood. In order to avoid the aforementioned error prone techniques, we endeavour to exploit the meshfree benefits of the LME approximants to introduce a node-linked method. Due to the global support of this interpolation technique, the classical interpretation of the FEM element typically adopted in MPM simulations is not required anymore. Instead, a linked list with the surrounding nodes for each node is defined at the initial time. Also, each particle has to be associated with the closest node instead with the belonging element as heretofore has been done. Now lets define the concept of a particle *tributary nodes* as the list of nodes close to it among which the information transfers occurs. Once the closest node are defined, the particle posses automatically a list of *tributary nodes*. This has two immediate benefits, the first is that shape functions with global support as LME are easier to implement, and the second is the increase of the efficiency of the  $\epsilon$ -neighbourhood reconstruction. Regarding this last benefit, since the current particle has a *tributary nodes* list assigned to it, and consequently each node has a linked list with a set of *tributary particles*<sup>4</sup> close to it, is possible to define efficiently a search list with those particles close to the current particle. In the end, particles out of the area of influence, Figure 1, are pop out of the final  $\epsilon$ -neighbourhood. A final remark about this new approach is its ability to reconstruct easily a search list with the support of the initial connectivity of the mesh. It provides a suitable basis for an easy implementation of other interpolation techniques with minimum coding effort. A detailed explanation of the proposed algorithm can be found in Appendix C.

---

<sup>4</sup>Notice that the list of the particles close to each node is unique for each node and is updated in each time step.

### 3. Cases of study and discussion

The proposed approach to overcome the two main shortcomings of Eigen-MPM [30] has been evaluated with “three benchmark tests”. The first one deals with the presence of stress instabilities provoked by the spatial discretization, appearing even when the GIMP shape functions are employed. To overcome it, LME approximants are introduced as an alternative to the existing interpolation techniques. Its performance in mitigating spurious stress oscillations under the MPM [43, 34] framework helps to enhance notoriously the quality of the results as it is observed in Section 3.1, where both interpolation techniques are compared by carrying out an eigenerosion simulation. The second limitation is concerned to its inability to simulate properly quasi-brittle fracture [39]. It can be solved through the eigensoftening algorithm described in Section 2.3. A proof of it is exposed in Sections 3.2 3.3, where experimental results are compared with experimental ones as well as eigensoftening computations. In the first case comparing with a semicircular bending test and in the second case with a drop-weight impact test.

#### 3.1. Edge-cracked square panel in mode I

The aim of the problem presented hereinafter is to assess the capability of the LME approximants to improve the result *versus* the standard linear interpolation. The application consists of a square plate of size  $H = 1 [L]$  containing an initial edge crack of length  $0.25 \cdot H$  loaded in a pure mode I by displacement control on the outer flanks of the plate (See Figure 3 for details). The constitutive model considered in the numerical experiment is a linear-elastic Hookean material, whose Young’s modulus  $E = 1.06 [M][L]^{-1}[T]^{-2}$ , the Poisson’s ratio  $\nu = 0.333$ , and critical energy-release rate  $G_F = 0.0001 [L]^2[T]^{-2}$ . The absence of units is due to the current simulation will not be validated against experimental results, where scale factor is relevant, but will be against an analytical solution provided by Pandolfi & Ortiz [29]. In MPM, two different discretization are required. On one hand, a cartesian grid of nodes is considered with a nodal spacing value of 0.025. On the other hand, the plate will be modeled with a initial layout of four particles per element and occupying the Gauss quadrature positions.

Figure 4 clearly shows the  $LME_{\gamma=3.5}$  solution has a reaction peak value of  $0.03 [M][L][T]^{-2}$  for a imposed displacement  $0.015 [L]$  which agrees with the analytical solution [29]. It also shows the presence of wiggles in the reaction-displacements curve, in both loading and post-failure stages, when linear interpolation technique is used. In contrast, LME simulation does not

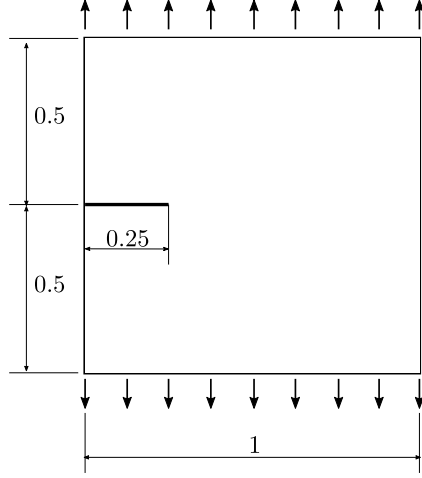


Figure 3: Geometry and boundary condition of the drop-weight impact test.

exhibit these spurious oscillations and remains linear until the failure. About the strength, linear interpolation produces stiffer results than LME. This can be attributed to imprecision in the stress field due to grid-crossing phenomena.

Additionally, Figure 5 exhibits more clearly the difference between linear interpolation and LME, since numerical instability becomes rather significant when particles cross the boundary of the element in the linear case, which is observed at 60 seconds. Although, apparently, the differences in the obtained peaks are not extremely significant, it can be owing to the aforementioned hookean material employed [30]. When more sophisticated constitutive models will be employed, severe inaccuracies may appear in the stress field that could affect dramatically to the final result. Focusing on the post failure behavior, it can be seen how LME produces soft stress field evolution even after breaking. An important consideration regarding the presence of oscillations once both parts of the panel are separated is observed in Figure 4. These phenomena should not be attributed to the eigenerosion algorithm since the fracture process is over. They are due to the dynamic nature of the solver: once the energy is release dinamically by the crack, the waves propagate along the domain.

### 3.2. Semicircular bending test

The second application to be considered is two semicircular bending tests on Johnstone, which have been carried out by Lim *et al.* [44] and numerically reproduced by Wang *et al.*[15] under SPH framework within an implicit algorithm. The aim of the test is to examine the predictive capability of the

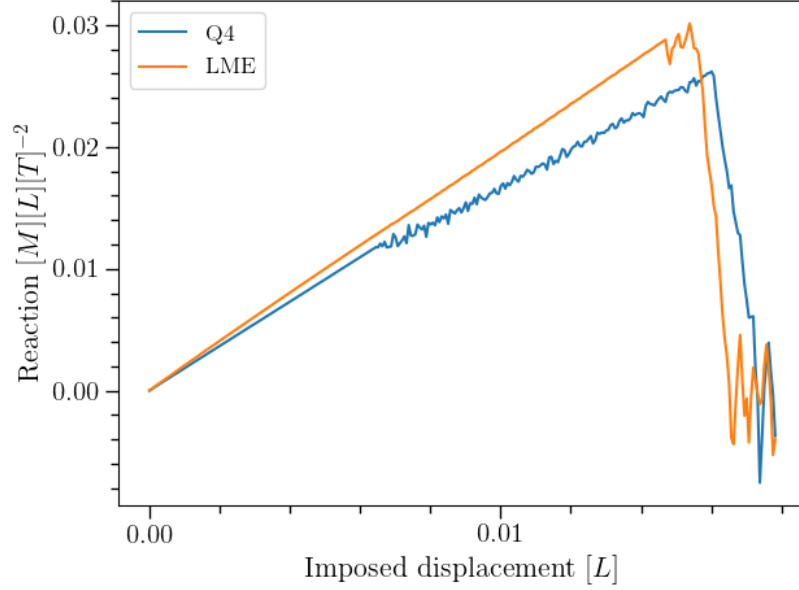


Figure 4: Evolution of the reaction forces plotted *versus* the imposed displacement for linear interpolation technique and the LME approximants.

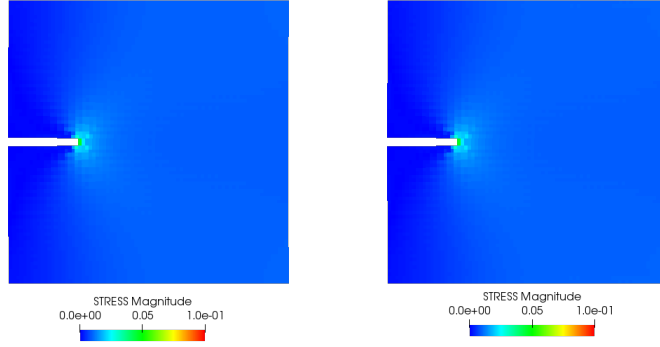
|   |               |
|---|---------------|
| Young's modulus ( $E$ )                 | 0.4 $GPa$     |
| Poisson ratio ( $\nu$ )                 | 0.25          |
| Density ( $\rho$ )                      | 1.54 $g/cm^3$ |
| Tensile strength ( $f_t$ )              | 0.6 $MPa$     |
| Critical opening displacement ( $w_c$ ) | 0.015 $mm$    |

Table 1: Material properties of Johnstone.

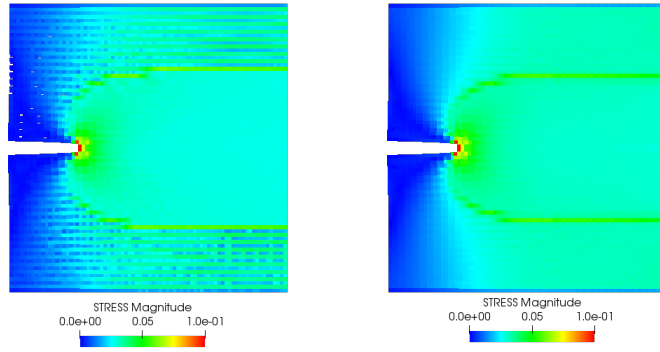
eigensoftening algorithm under different kind of mixed-mode loading conditions. This capability was previously within a OTM implementation [39].

The geometry and boundary conditions are sketched in Figure 6. The experiment consist in two semicircular specimens with a radius of 47.5 mm and a thickness of 20 mm are supported by two rollers at a span of 47.5 mm and loaded by another roller on its mid-span. Notches with a length of 16.6 mm are created with different notch angles of 0 and 60 with respect to the vertical axis to investigate the influences of the notch angles on the peak load. The material properties of Johnstone are listed in Table 1.

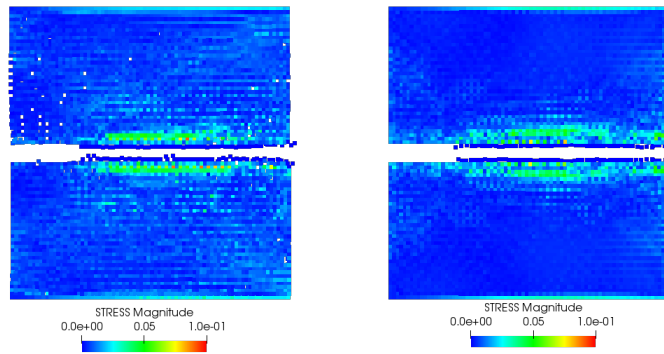
In the tests, particles were uniformly distributed with an almost constant separation of 1 mm between them, resulting in a total number of 4672 MPM particles for generating the specimen. Additionally a regular cartesian background grid of 1917 nodes with 1.5 mm of nodal distance was generated.



(a)  $t = 25$



(b)  $t = 60$



(c)  $t = 100$

Figure 5: Evolution of the stress tensor magnitude for linear interpolation (pictures in the left side), and LME (pictures in the right side). Both simulations performed with an eigenerosion algorithm.

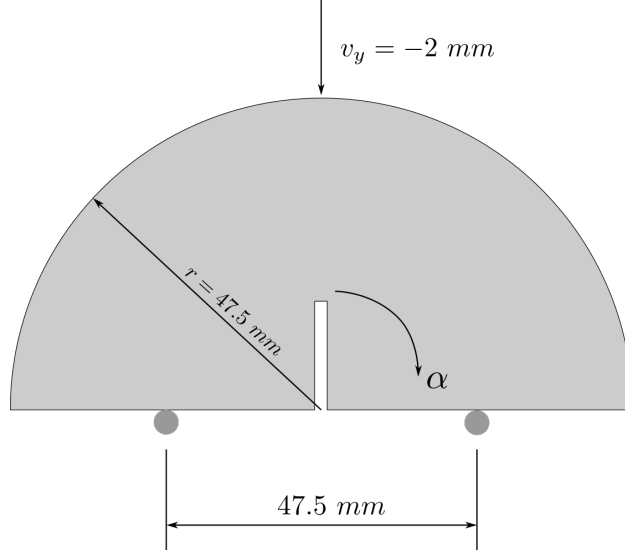


Figure 6: Geometry and boundary condition of the semicircular bending test.

### 3.3. Drop-weight impact test

240 This section is devoted to proof the accuracy of the eigensoftening algo-  
 rithm within the MPM framework when the behavior of quasi-brittle ma-  
 terials under dynamic loading is simulated. One of the most interesting  
 examples of this loading case is the three-point bending test on a concrete  
 245 notched beam when it is conducted under impact loading. Indeed, this ex-  
 perimental test is appropriate to be reproduced numerically with the explicit  
 solver proposed in this paper since fracture occurs in a period of milliseconds  
 and waves propagate fast along the high strength materials involved in the  
 aforementioned test. Accordingly, small time steps are required to achieve  
 a numerically stable simulation.

250 An interesting case of this experimental test was reported by Zhang *et al.*  
 [45, 46]. As in the aforementioned study, an impact hammer of 120.6 kg has  
 been employed in the proposed simulations to drop it at an impact speed of  
 881 mm/s. The beam dimensions were 100 mm x 100 mm (B x D) in cross  
 255 section, and 420 mm in total length (L). The initial notch-depth ratio was  
 approximately 0.5, and the span, S, was fixed at 300 mm during the tests  
 (see Figure 7). The material adopted for the simulation was characterised by  
 Navas *et al.* [31], being the material properties, such as the material density,  
 $\rho$ , the compressive strength,  $f_c$ , the tensile strength  $f_t$ , the specific fracture  
 260 energy,  $G_F$ , and the elastic modulus E, provided in table 2.

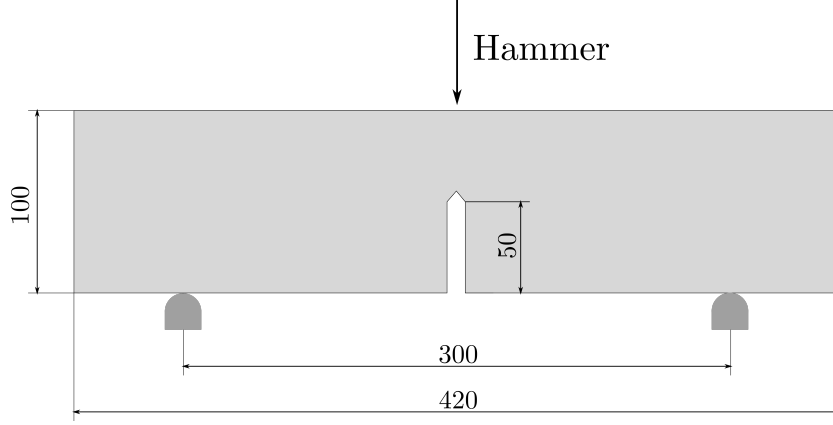


Figure 7: Geometry and boundary condition of the drop-weight impact test.

|       | $\rho$<br>(kg/m <sup>3</sup> ) | $f_c$<br>(MPa) | $f_t$<br>(MPa) | $G_F$<br>(N/m) | E<br>(GPa) | $d_{max}$<br>(mm) |
|-------|--------------------------------|----------------|----------------|----------------|------------|-------------------|
| Value | 2368                           | 102.7          | 5.4            | 141            | 31         | 12                |

Table 2: Mechanical properties of the high strenght concrete.

For the present research, a 2D setting of the experiment has been adopted. Both the hammer and the concrete beam are explicitly represented in order to properly capture the impact. Several levels of discretization were required to assess the objectiveness of the obtained results. The results here exposed are from a discretization of 30616 material points and 6297 nodes. To achieve better results, an unstructured grid layout has been adopted focusing the minimum nodal spacing, 0.47 mm, in the middle of the beam and in the impact surface of the hammer. For this simulation,  $\hat{\gamma}$  was fixed to 6. Once the accuracy of the LME approximants have been proven in Section 3.1, this discretization has been adopted.

First, the reaction and impact forces are validated against their experimental counterparts. Since the impact forces applied by the hammer and the reaction forces at the two supports were experimentally measured, they are compared with numerical ones in Figure 8. Note that the general trend of both forces are correctly captured. Observe that in experimental solution the delay between impact peak and reactions peak does not agree with the numerical ones. On the other hand, if the delay is computed analytically through concrete wave speed is much closer to the numerical results. A feasible explanation to this unexpected result can due the composite nature of the concrete. Another discrepancy is in the much higher values of maximum impact and reaction forces in numerical than in experimental. In this case,



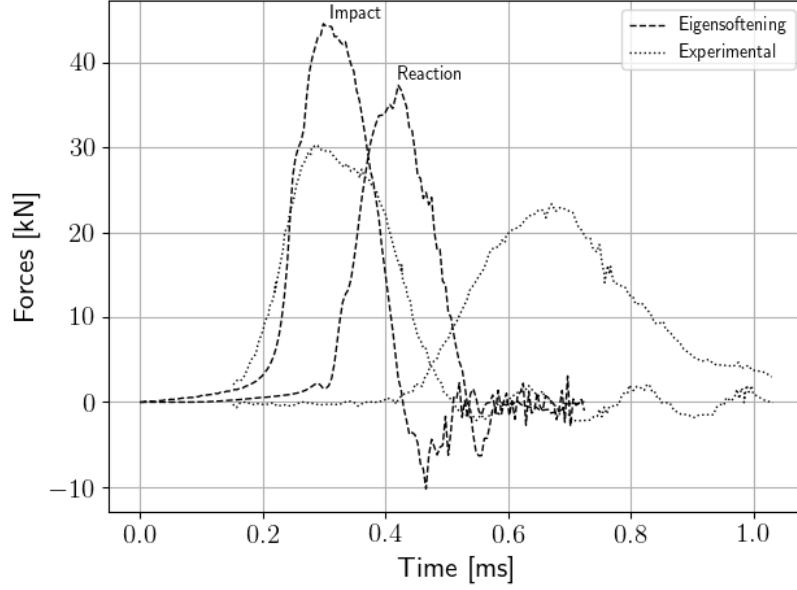
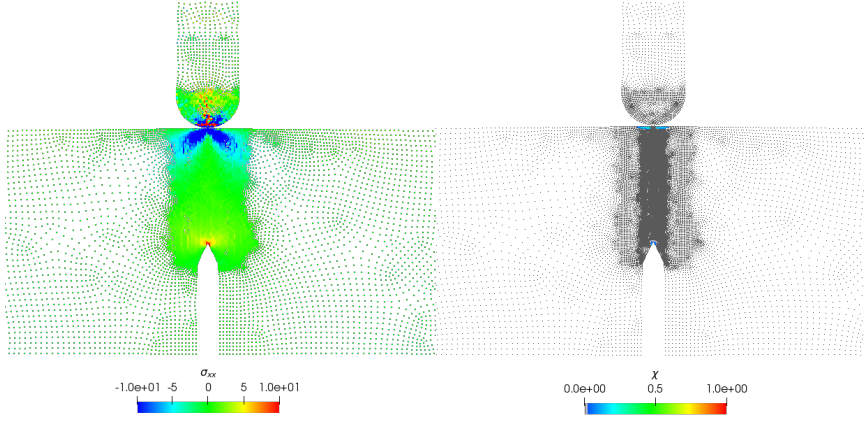


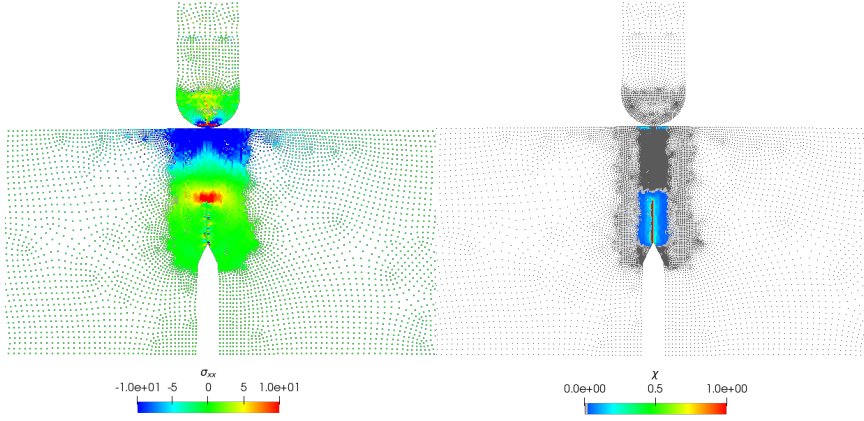
Figure 8: Evolution of the reaction forces plotted *versus* the imposed displacement for linear interpolation technique and the LME approximants.

this is a consequence of over-rigidity in the supports. Although the traditional MPM implementation allows collision of two bodies, inaccurate energy conservation is obtained without the implementation of a conservative contact algorithm to reproduce the hammer impact in the beam. Despite the observed discrepancies, this is out of the scope of this document, although future research of authors will overcome this limitation. Similarly, results of support forces will be more realistic when modelled by a suitable contact algorithm instead of avoiding any vertical displacement .

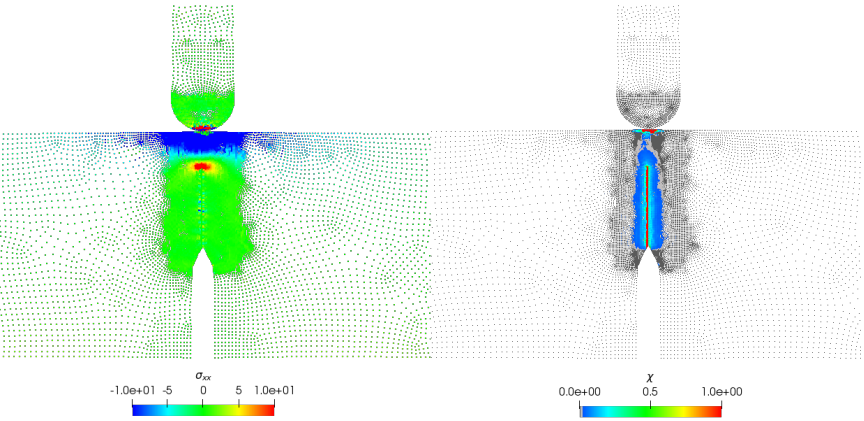
Finally, longitudinal stress distribution and crack propagation are depicted in Figure 9. Stress evolution agrees with the results obtained by [31] under the OTM framework. Two additional considerations about this results are concerning the interpolation technique. On the one hand, in the opposite to the uGIMP shape function, LME allows unstructured grids. This is a remarkable benefit for this kind of simulations since the majority of the computational effort is clearly localised in a tiny region of the domain. On the other hand, there is the possibility to reduce the shape function support to avoid a material point in one side of the crack is affected by those in the other side of the crack.



(a)  $t = 0.27$  ms



(b)  $t = 0.36$  ms



(c)  $t = 0.45$  ms

Figure 9: Evolution of the stress tensor magnitude for linear interpolation (pictures in the left side), and LME (pictures in the right side). Both simulations performed with an eigenerosion algorithm.

## 4. Conclusions

Firstly, by introducing the concept of eigensoftening to the MPM framework, which allows to consider gradual failure process of each material point. This concept is analogous the softening law which is traditionally employed in the context of cohesive fracture in Finite Element Method (FEM). Furthermore, this failure criterion admits the design of more elaborated damage curves, which can be employed in order to describe the failure process in more sophisticated materials. In this direction, an interesting future improvement of the algorithm would be the ability to simulate of crack patterns in composite material such as steel or carbon fiber reinforced concretes[47]. Interesting researches have been done on this field [39]. In addition, the eigensoftening approach can be extrapolated to rock fracture in the same manner the eigen-erosion was [48], taking into account that the volumetric stiffness remains in order to support bulk loads.

Secondly, LME is employed to remove from the solution those wiggles provoked by inaccuracies in the stress integration. This spatial discretization was previously employed within the MPM framework with excellent results under the elastic regime [43, 34]. The traditional time scheme of the MPM has been improved with a Newmark Predictor Corrector scheme as well. In this research, the aforementioned techniques have helped to improve the results in fracture propagation through the eigensoftening and eigen-erosion algorithms. Further improvement may be reached by adapting LME through the deformation gradient [49]. *A priori* this would enhance the localisation properties of the proposed algorithms in more sophisticated domains.

Finally, for better capturing the measurement of forces made in the laboratory, more realistic contact tools have to be developed. Navas et al. demonstrate the importance of the stiffness of the support in order to obtain accurate results of the reaction forces. Interesting contact algorithms within the MPM methodology are available in the literature [50, 51]

## Acknowledgements

The financial support to develop this research from the Ministerio de Ciencia e Innovación, under Grant No. BIA-2016-76253 is greatly appreciated. The first and the second authors also acknowledge the fellowship Fundación Agustín de Betancourt and Juan de la Cierva (FJCI-201731544) respectively.



## Appendix A. Explicit Newmark Predictor-Corrector algorithm

1 **Update mass matrix :**  $\mathbf{m}_I = N_{Ip}^k m_p$

2 **Explicit Newmark Predictor :**

$$\vec{v}_I^{pred} = \frac{N_{Ip}^k m_p (\vec{v}_p^k + (1 - \gamma) \Delta t \vec{a}_p^k)}{m_I}$$

3 **Impose essential boundary conditions :** At the fixed boundary, set  $\vec{v}_I^{pred} = 0$ .

4 **Deformation tensor increment calculation :**

$$\Delta \varepsilon_p^{k+1} = \Delta t \dot{\varepsilon}_p^{k+1} = \Delta t \left[ \vec{v}_I^{pred} \otimes \text{grad}(N_{Ip}^{k+1}) \right]^s$$

5 **Update the density field :**  $\rho_p^{k+1} = \frac{\rho_p^k}{1 + \text{tra}[\Delta \varepsilon_p^{k+1}]}$ .

6 **Compute stress field and update damage parameter**

7 **Balance of forces calculation :** Calculate the total grid nodal force  $\vec{f}_I^{k+1} = \vec{f}_I^{int,k+1} + \vec{f}_I^{ext,k+1}$ .

8 **Explicit Newmark Corrector :**

$$\vec{v}_I^{k+1} = \vec{v}_I^{pred} + \gamma \Delta t \frac{\vec{f}_I^{k+1}}{\mathbf{m}_I^{k+1}}$$

9 **Update particles lagrangian quantities :**

$$\vec{a}_p^{k+1} = \frac{N_{Ip}^k \vec{f}_I^k}{\mathbf{m}_I^k}$$

$$\vec{v}_p^{k+1} = \vec{v}_p^k + \Delta t \frac{N_{Ip}^k \vec{f}_I^k}{\mathbf{m}_I^k}$$

$$\vec{x}_p^{k+1} = \vec{x}_p^k + \Delta t N_{Ip}^k \vec{v}_I^k + \frac{1}{2} \Delta t^2 \frac{N_{Ip}^k \vec{f}_I^k}{\mathbf{m}_I^k}$$

10 **Reset nodal values**

**Algorithm 1:** Explicit Newmark Predictor-Corrector scheme

## Appendix B. Eigensoftening Algorithm

**Input:** For each  $p$ ,  $\epsilon$ -neighbourhood,  $f_{t,p}$ ,  $h_{\epsilon,p}$ ,  $w_c$   
**Output:** Return damage parameter  $\chi := \{\chi_p\}$

```

1  $\chi_p \leftarrow \chi_p^k$ 
2 for  $p$  to  $N_p$  do
3   if  $\chi_p = 0$   $\epsilon_{f,p} = 0$  then
4     for  $q \in B_{\epsilon,p}$  do
5        $\sigma_{q,I} \leftarrow \text{getEigenvaluesOf}(\sigma_q)$ 
6       if  $\chi_q < 1$  then
7          $\sum m_p \sigma_{p,I} \leftarrow \sum m_p \sigma_{p,I} + m_q \sigma_{q,I}$ 
8       end
9        $m_p \leftarrow m_p + m_q$ 
10    end
11     $\sigma_{p,\epsilon} \leftarrow \frac{1}{m_p} \sum m_p \sigma_{p,I}$ 
12    if  $\sigma_{p,\epsilon} > f_{t,p}$  then
13       $\epsilon_{f,p} = \epsilon_{I,p}$ 
14    end
15    else if  $\chi_p \neq 1$   $\epsilon_{f,p} > 0$  then
16       $\chi_p^{k+1} \leftarrow \min \left\{ 1, \max \left\{ \chi_p^k, \frac{(\epsilon_{I,p} - \epsilon_{f,p})}{w_c} h_{\epsilon,p} \right\} \right\}$ 
17    end
18  end
19 end

```

**Algorithm 2:** Compute damage parameter  $\chi_p^{k+1}$

## Appendix C. Node-linked method for $\epsilon$ -neighbourhood reconstruction

|    |   |
|----|---|
|    | <b>Input:</b> $I_0$ : Closest node for each particle                                  |
|    | <b>Input:</b> $I_{Nodes}$ : List of nodes close to each node                          |
|    | <b>Input:</b> $Particles_I$ : List of particles close to each node                    |
|    | <b>Output:</b> $neighbourhood_\epsilon$ : $\epsilon$ -neighbourhood for each particle |
| 1  | <b>for</b> $p$ to $N_p$ <b>do</b>   |
| 2  | For each $p$ get $I_0$  |
| 3  | Eval $I_{Nodes}(I_0)$   |
| 4  | <b>for</b> $k \in I_{Nodes}(I_0)$ <b>do</b>   |
| 5  | $neighbourhood_\epsilon^{k+1} = neighbourhood_\epsilon^k \cup Particles_I(k)$         |
| 6  | <b>end</b>  |
| 7  | <b>for</b> $p_\epsilon \in neighbourhood_\epsilon$ <b>do</b>                          |
| 8  | <b>if</b> $distance(p_\epsilon, p) > \epsilon$ <b>then</b>                            |
| 9  | pop $p_\epsilon$ from $neighbourhood_\epsilon$  |
| 10 | <b>end</b>  |
| 11 | <b>end</b>  |
| 12 | <b>end</b>  |

**Algorithm 3:**  $\epsilon$ -neighborhood reconstruction algorithm

## References

- [1] G. Barenblatt, The mathematical theory of equilibrium cracks in brittle fracture., *Advances in Applied Mechanics* 7 (1962) 55–129.
- [2] A. Hillerborg, M. Mod  r, P. Petersson, Analysis of crack formation and crack growth in concrete by means of fracture mechanics and finite elements., *Cement and Concrete Research*. 6 (1976) 773–782.
- [3] M. Ortiz, A. Pandolfi, Finite-deformation irreversible cohesive elements for three-dimensional crack-propagation analysis., *International Journal for Numerical Methods in Engineering*. 44 (1999) 1267–1282.
- [4] A. Pandolfi, M. Ortiz, An efficient adaptive procedure for three-dimensional fragmentation simulations., *Engineering with Computers*. 18(2) (2002) 148–159.
- [5] G. Ruiz, M. Ortiz, A. Pandolfi, Three-dimensional finite-element simulation of the dynamic Brazilian tests on concrete cylinders, *International Journal for Numerical Methods in Engineering* 48 (2000) 963–994.

- 360 [6] T. Belytschko, H. Chen, J. Xu, G. Zi, Dynamic crack propagation based on loss of hyperbolicity and a new discontinuous enrichment., *International Journal for Numerical Methods in Engineering*. 58 (2003) 1873–1905.
- [7]
- 365 [8] Z. Chen, W. Hu, L. Shen, X. An, R. Brannon, An evaluation of the mpm for simulating dynamic failure with damage diffusion, *Engineering Fracture Mechanics* 69 (2002) 1873–1890. doi:10.1016/S0013-7944(02)00066-8.
- 370 [9] J. Nairn, Material point method calculations with explicit cracks, *Computer Modeling in Engineering & Sciences* 4 (6) (2003) 649–664. doi:10.3970/cmcs.2003.004.649.  
URL <http://www.techscience.com/CMES/v4n6/33290>
- [10] Z. Chen, L. Shen, Y.-W. Mai, Y.-G. Shen, A bifurcation-based decohesion model for simulating the transition from localization to decohesion with the mpm, *Zeitschrift fur Angewandte Mathematik und Physik* 56 (2005) 908–930. doi:10.1007/s00033-005-3011-0.
- 375 [11] T. Belytschko, Y. Lu, L. Gu, M. Tabbara, Element-free galerkin methods for static and dynamic fracture, *International Journal of Solids and Structures* 32 (17) (1995) 2547 – 2570. doi:[https://doi.org/10.1016/0020-7683\(94\)00282-2](https://doi.org/10.1016/0020-7683(94)00282-2).  
380 URL <http://www.sciencedirect.com/science/article/pii/S0020768394002822>
- [12] T. Belytschko, D. Organ, C. Gerlach, Element-free galerkin methods for dynamic fracture in concrete, *Computer Methods in Applied Mechanics and Engineering* 187 (3) (2000) 385 – 399. doi:[https://doi.org/10.1016/S0045-7825\(00\)80002-X](https://doi.org/10.1016/S0045-7825(00)80002-X).  
385 URL <http://www.sciencedirect.com/science/article/pii/S004578250080002X>
- [13] X. Zhuang, C. Augarde, K. Mathisen, Fracture modeling using meshless methods and level sets in 3d: Framework and modeling, *International Journal for Numerical Methods in Engineering* 92 (2012) 969–998. doi:10.1002/nme.4365.
- 390 [14] N. Muthu, S. Maiti, B. Falzon, I. Guiamatsia, A comparison of stress intensity factors obtained through crack closure integral and other ap-



- proaches using extended element-free galerkin method, Computational Mechanics 52. doi:10.1007/s00466-013-0834-y.
- [15] Y. Wang, H. T. Tran, G. D. Nguyen, P. G. Ranjith, H. H. Bui, Simulation of mixed-mode fracture using sph particles with an embedded fracture process zone, International Journal for Numerical and Analytical Methods in Geomechanics n/a (n/a). arXiv: <https://onlinelibrary.wiley.com/doi/pdf/10.1002/nag.3069>, doi:10.1002/nag.3069.  
URL <https://onlinelibrary.wiley.com/doi/abs/10.1002/nag.3069>
- [16] Y. Wang, H. Bui, G. Nguyen, P. Ranjith, A new sph-based continuum framework with an embedded fracture process zone for modelling rock fracture, International Journal of Solids and Structures 159 (2019) 40–57. doi:10.1016/j.ijsolstr.2018.09.019.
- [17] B. Li, F. Habbal, M. Ortiz, Optimal transportation meshfree approximation schemes for fluid and plastic flows, International Journal for Numerical Methods in Engineering 83 (12) (2010) 1541–1579. doi:10.1002/nme.2869.  
URL <http://doi.wiley.com/10.1002/nme.2869>
- [18] B. Li, A. Kadane, G. Ravichandran, M. Ortiz, Verification and validation of the optimal-transportation meshfree (otm) simulation of terminal ballistics., International Journal for Impact Engineering 42 (2012) 25–36.
- [19] A. Pandolfi, B. Li, M. Ortiz, Modeling fracture by material-point erosion., International Journal of fracture 184 (2013) 3–16.
- [20] B. Li, A. Pandolfi, M. Ortiz, Material-point erosion simulation of dynamic fragmentation of metals., Mechanics of Materials 80 (2015) 288–297.
- [21] Y. D. Ha, F. Bobaru, Characteristics of dynamic brittle fracture captured with peridynamics, Engineering Fracture Mechanics 78 (6) (2011) 1156 – 1168. doi:<https://doi.org/10.1016/j.engfracmech.2010.11.020>.  
URL <http://www.sciencedirect.com/science/article/pii/S0013794410004959>
- [22] T. Rabczuk, H. Ren, A peridynamics formulation for quasi-static fracture and contact in rock, Engineering Geology 225

- 430 (2017) 42 – 48, special Issue: Characterisation of Fractures in  
Rock: from Theory to Practice (ROCKFRAC). doi:<https://doi.org/10.1016/j.enggeo.2017.05.001>.  
URL <http://www.sciencedirect.com/science/article/pii/S0013795217306907>
- 435 [23] Y. GUO, J. Nairn, Three-dimensional dynamic fracture analysis using  
the material point method, *Computer Modeling in Engineering Sciences*  
16.
- [24] H. Tan, J. Nairn, Hierarchical, adaptive, material point method for  
dynamic energy release rate calculations, *Computer Methods in Ap-  
plied Mechanics and Engineering* 191 (2002) 2123–2137. doi:10.1016/  
440 S0045-7825(01)00377-2.
- [25] Y. GUO, J. Nairn, Calculation of j-integral and stress intensity factors  
using the material point method, *CMES. Computer Modeling in Engi-  
neering Sciences* 6.
- 445 [26] Z. Chen, R. Feng, X. An, L. Shen, A computational model for impact  
failure with shearinduced dilatancy, *International Journal for Numerical  
Methods in Engineering* 56 (2003) 1979 – 1997. doi:10.1002/nme.651.
- [27] S. DL, L. Schreyer, Mpm simulation of dynamic material failure with  
a decohesion constitutive model, *European Journal of Mechanics -  
A/Solids* 23 (2004) 423–445. doi:10.1016/j.euromechsol.2004.02.  
450 007.
- [28] B. Schmidt, F. Fraternali, M. Ortiz, Eigenfracture: an eigendeformation  
approach to variational fracture., *SIAM J. Multiscale Model. Simul.* 7  
(2009) 1237–1266.
- 455 [29] A. Pandolfi, M. Ortiz, An eigenerosion approach to brittle fracture.,  
*International Journal for Numerical Methods in Engineering* 92 (2012)  
694–714.
- [30] K. Zhang, S.-L. Shen, A. Zhou, Dynamic brittle fracture with  
eigenerosion enhanced material point method, *International Jour-  
nal for Numerical Methods in Engineering* n/a (n/a). arXiv:  
460 <https://onlinelibrary.wiley.com/doi/pdf/10.1002/nme.6381>,  
doi:10.1002/nme.6381.  
URL <https://onlinelibrary.wiley.com/doi/abs/10.1002/nme.6381>

- 465 [31] P. Navas, R. Yu, B. Li, G. Ruiz, Modeling the dynamic fracture in concrete: an eigensoftening meshfree approach, *International Journal of Impact Engineering* 113. doi:10.1016/j.ijimpeng.2017.11.004.
- [32] P. Navas, S. López-Querol, R. C. Yu, M. Pastor, Optimal transportation meshfree method in geotechnical engineering problems under large  
470 deformation regime, *International Journal for Numerical Methods in Engineering* doi:10.1002/nme.5841.
- [33] Z. Bažant, B. Oh, Crack band theory for fracture in concrete., *Materials and Structures*. 16 (1983) 155–177.
- [34] M. Molinos, P. Navas, M. Pastor, M. Martín Stickle, On the dynamic  
475 assessment of the Local-Maximum Entropy Material Point Method through an Explicit Predictor-Corrector Scheme, *Computer Methods in Applied Mechanics and Engineering* Under review (2020) –.
- [35] M. Arroyo, M. Ortiz, Local maximum-entropy approximation schemes: A seamless bridge between finite elements and meshfree methods, Inter-  
480 national Journal for Numerical Methods in Engineering doi:10.1002/nme.1534.
- [36] D. L. Sulsky, H. Schreyer, Z. Chen, A particle method for history-dependent materials, *Computer Methods in Applied Mechanics and Engineering* 118 (1) (1994) 179–196. doi:10.1016/0045-7825(94)  
485 90112-0.
- [37] E. Jaynes, Information Theory and Statistical Mechanics, *The Physical Review* 106 (4) (1957) 620–630.
- [38] C. E. Shannon, A Mathematical Theory of Communication, *Bell System Technical Journal* doi:10.1002/j.1538-7305.1948.tb01338.x.
- 490 [39] P. Navas, R. Yu, G. Ruiz, Meshfree modeling of the dynamic mixed-mode fracture in frc through an eigensoftening approach, *Engineering Structures* 172. doi:10.1016/j.engstruct.2018.06.010.
- [40] M. P. Allen, D. J. Tildesley, *Computer Simulation of Liquids*, Clarendon Press, USA, 1989.
- 495 [41] M. Shimrat, Algorithm 112: Position of point relative to polygon, *Commun. ACM* 5 (8) (1962) 434. doi:10.1145/368637.368653.  
URL <https://doi.org/10.1145/368637.368653>

- [42] M. Galetzka, P. Glauner, A simple and correct even-odd algorithm for the point-in-polygon problem for complex polygons, 2017. doi: 10.5220/0006040801750178.
- [43] E. Wobbes, R. Tielen, M. Möller, C. Vuik, Comparison and unification of material-point and optimal transportation meshfree methods, Computational Particle Mechanics doi:10.1007/s40571-020-00316-7.
- [44] I. Lim, I. Johnston, S. Choi, Stress intensity factors for semi-circular specimens under three-point bending, Engineering Fracture Mechanics 44 (3) (1993) 363 – 382. doi:https://doi.org/10.1016/0013-7944(93)90030-V. URL <http://www.sciencedirect.com/science/article/pii/S001379449390030V>
- [45] X. Zhang, G. Ruiz, R. Yu, M. Tarifa, Fracture behaviour of high-strength concrete at a wide range of loading rates., International Journal of Impact Engineering 36 (2009) 1204–1209.
- [46] X. Zhang, R. Yu, G. Ruiz, M. Tarifa, M. Camara, Effect of loading rate on crack velocities in hsc., International Journal of Impact Engineering 37 (2010) 359–370.
- [47] G. Ruiz, A. [de la Rosa], L. Almeida, E. Poveda, X. Zhang, M. Tarifa, Z. Wu, R. Yu, Dynamic mixed-mode fracture in scc reinforced with steel fibers: an experimental study, International Journal of Impact Engineering 129 (2019) 101 – 111. doi:https://doi.org/10.1016/j.ijimpeng.2019.03.003. URL <http://www.sciencedirect.com/science/article/pii/S0734743X18309977>
- [48] K. Wang, W. Sun, A unified variational eigen-erosion framework for interacting brittle fractures and compaction bands in fluid-infiltrating porous media, Computer Methods in Applied Mechanics and Engineering 318 (2017) 1 – 32. doi:https://doi.org/10.1016/j.cma.2017.01.017. URL <http://www.sciencedirect.com/science/article/pii/S0045782516311537>
- [49] S. Kumar, K. Danas, D. M. Kochmann, Enhanced local maximum-entropy approximation for stable meshfree simulations, Computer Methods in Applied Mechanics and Engineering doi:10.1016/j.cma.2018.10.030.

- 535 [50] S. Bardenhagen, J. Guilkey, K. Roessig, J. Brackbill, W. Witzel, J. Foster, An improved contact algorithm for the material point method and application to stress propagation in granular material, CMES. Computer Modeling in Engineering Sciences 2. doi:10.3970/cmes.2001.002.509.
- 540 [51] P. Huang, X. Zhang, S. Ma, X. Huang, Contact algorithms for the material point method in impact and penetration simulation, International Journal for Numerical Methods in Engineering 85 (2011) 498 – 517. doi:10.1002/nme.2981.